

PAPER • OPEN ACCESS

Ghost anti-crossings caused by interlayer umklapp hybridization of bands in 2D heterostructures

To cite this article: Abigail J Graham *et al* 2021 *2D Mater.* **8** 015016

View the [article online](#) for updates and enhancements.

You may also like

- [Two-dimensional phonon transport in graphene](#)
Denis L Nika and Alexander A Balandin
- [Phonon hydrodynamics in crystalline materials](#)
Kanka Ghosh, Andrzej Kusiak and Jean-Luc Battaglia
- [Wide-range \$T^2\$ resistivity and umklapp scattering in moiré graphene](#)
Hiroaki Ishizuka and Leonid Levitov



PAPER

OPEN ACCESS

RECEIVED

23 August 2020

REVISED

23 September 2020

ACCEPTED FOR PUBLICATION

14 October 2020

PUBLISHED

30 October 2020

Original content from this work may be used under the terms of the [Creative Commons Attribution 4.0 licence](#).

Any further distribution of this work must maintain attribution to the author(s) and the title of the work, journal citation and DOI.



Ghost anti-crossings caused by interlayer umklapp hybridization of bands in 2D heterostructures

Abigail J Graham¹, Johanna Zultak^{2,3} , Matthew J Hamer^{2,3}, Viktor Zolyomi^{2,3}, Samuel Magorrian^{2,3}, Alexei Barinov⁴, Viktor Kandyba⁴, Alessio Giampietri⁴, Andrea Locatelli⁴, Francesca Genuzio⁴, Natalie C Deutsch¹, Cuauhtémoc Salazar¹, Nicholas D M Hine¹, Vladimir I Fal'ko^{2,3,5}, Roman V Gorbachev^{2,3,5} and Neil R Wilson¹

¹ Department of Physics, University of Warwick, Coventry CV4 7AL, United Kingdom

² National Graphene Institute, University of Manchester, Booth St East, Manchester M13 9PL, United Kingdom

³ School of Physics and Astronomy, University of Manchester, Oxford Road, Manchester M13 9PL, United Kingdom

⁴ Elettra – Sincrotrone Trieste, S.C.p.A, Basovizza (TS), 34149, Italy

⁵ Henry Royce Institute, Oxford Road, Manchester M13 9PL, United Kingdom

E-mail: Vladimir.Falko@manchester.ac.uk, Roman@manchester.ac.uk and Neil.Wilson@warwick.ac.uk

Keywords: ARPES, 2D materials, 2D heterostructures, umklapp scattering, twistrionics

Supplementary material for this article is available [online](#)

Abstract

In two-dimensional heterostructures, crystalline atomic layers with differing lattice parameters can stack directly one on another. The resultant close proximity of atomic lattices with differing periodicity can lead to new phenomena. For umklapp processes, this opens the possibility for interlayer umklapp scattering, where interactions are mediated by the transfer of momenta to or from the lattice in the neighbouring layer. Using angle-resolved photoemission spectroscopy to study a graphene on InSe heterostructure, we present evidence that interlayer umklapp processes can cause hybridization between bands from neighbouring layers in regions of the Brillouin zone where bands from only one layer are expected, despite no evidence for Moiré-induced replica bands. This phenomenon manifests itself as ‘ghost’ anti-crossings in the InSe electronic dispersion. Applied to a range of suitable two-dimensional material pairs, this phenomenon of interlayer umklapp hybridization can be used to create strong mixing of their electronic states, giving a new tool for twist-controlled band structure engineering.

1. Introduction

Crystalline periodicity modifies the interpretation of the momentum conservation law for electronic and optical processes in solids. It gives rise to a periodicity of the electronic dispersion in momentum space, so that, according to Bloch's theorem [1], the band-structure is uniquely defined within one (the first) Brillouin zone. All processes in a crystal can then be divided into two types: those with small momentum differences that can be described within the first Brillouin zone and those where a large momentum transfer requires the involvement of other Brillouin zones. In the latter case, a momentum transfer $\hbar G$ to the crystalline lattice, where G is one of the reciprocal lattice vectors, satisfies the conservation of momentum and was dubbed *Umklappprozesse* (Umklapp processes) by Peierls [2]. When applied to heterostructures of two-dimensional materials (2DMs),

umklapp scattering from Moiré superlattices has been shown to open new channels for electron kinetics [3] and optical transitions [4].

2DMs represent a broad class of compounds where atomic planes formed by strong in-plane covalent bonding are held together by a weak van der Waals interaction. These weak out-of-plane forces enable the stacked assembly of 2DM heterostructures (2DHSs), where consecutive layers may involve atomic planes of different compounds with arbitrary lattice constants and orientation, with atomically clean interfaces [5–7] which allow neighbouring layers in the heterostructure to influence each other, in particular through tunnelling. Tunnelling across clean interfaces is subject to momentum conservation [8, 9], so that it is resonantly enhanced in the part of momentum space where the bands of two 2DM intersect, causing resonant interlayer hybridization. Dramatic bandstructure modifications through resonant

interlayer hybridization have been studied in twisted bilayers of graphene [10–12], graphene on single-crystal metal substrates [13, 14], and graphene with other 2DM [15, 16], leading to band anti-crossings and, potentially, to van Hove singularities in the density of states. Here, we demonstrate that interlayer umklapp processes in resonant tunnelling lead to the appearance of additional features in the hybridized band structures of 2DHS.

2. Results and discussion

An example of such an effect is illustrated in figure 1, where angle-resolved photoemission spectroscopy with submicrometre spatial resolution (μ ARPES) has been used to probe the valence band structure in a graphene on InSe 2DHS. In figure 1(b) we sketch the valence band dispersion of monolayer InSe (unfolded over the second Brillouin zone replicas marked by $\mu = 0, 1 \dots 5$) and the π bands of graphene. Notably, no interlayer band crossing occurs in the first Brillouin zone of InSe so one would not expect any resonant hybridization of electronic states (and hence anti-crossing features) in the InSe monolayer spectrum. We find no evidence for replica bands due to a Moiré superlattice potential. Nonetheless, the measured μ ARPES spectrum features a pronounced anti-crossing anomaly near the edge of the valence band, as highlighted by a black box in figure 1(a), showing the photoemitted intensity in an energy-momentum slice taken along the Γ to K_{Gr} direction. This ‘ghost’ anti-crossing occurs due to interlayer umklapp hybridization where resonance conditions are achieved by the band crossing between graphene and InSe dispersions in the second Brillouin zone of InSe, also present in the measured spectra of graphene bands (see the purple box in figure 1(a)).

The 2DHSs studied in this work were assembled by dry transfer in an inert environment, where exfoliated crystals of InSe and GaSe were deposited on thick graphite and encapsulated with monolayer graphene (see Methods and schematic inset in figure 1(b)). This method allows for ARPES probing of buried layers through graphene (as graphene’s ARPES spectrum is already well known [17, 18]) while allowing for surface charge dissipation into a conductive substrate (platinum-coated n-Si wafer) [19]. Several samples were fabricated using different thicknesses of InSe and GaSe crystals, and different twist angles with respect to the graphene lattice.

The ghost anti-crossings, and their origin, are more apparent when looking across reciprocal space. The photoemission intensity at a constant energy near the top of the InSe upper valence band (UVB), in a region around Γ , is shown in figure 2(a) and reveals the twisted lines in reciprocal space at which the ghost anti-crossings occur. The measured data (black dashed rectangle) have been averaged and rotated to form the complete image, as described in

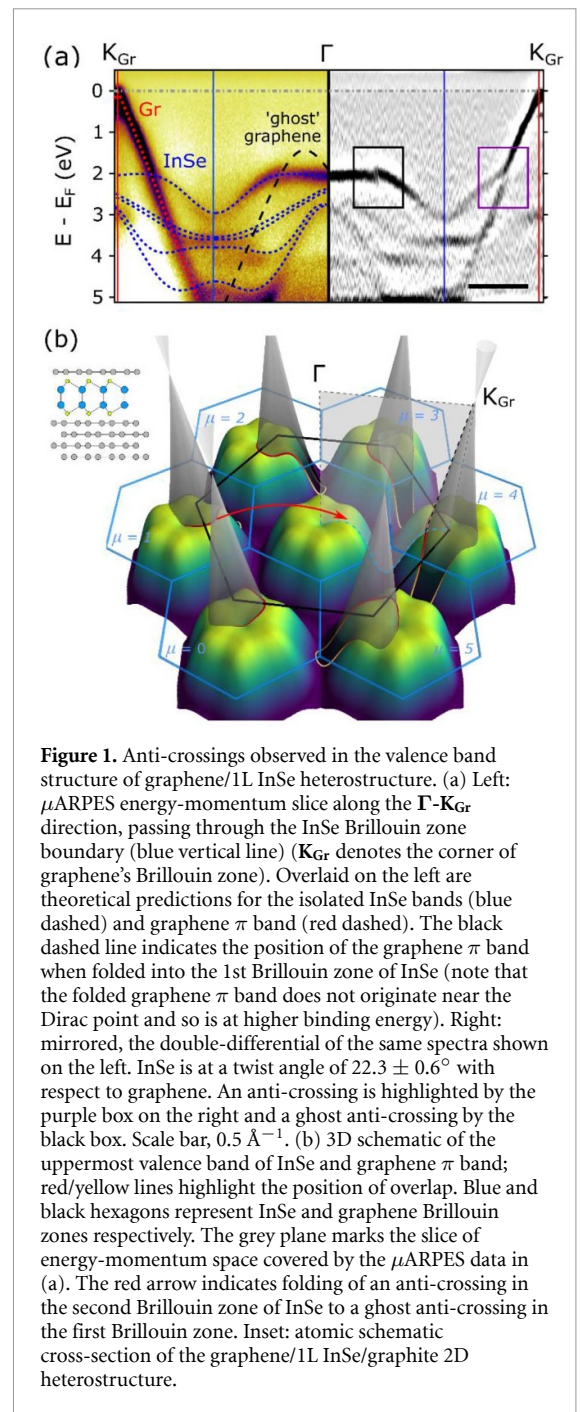
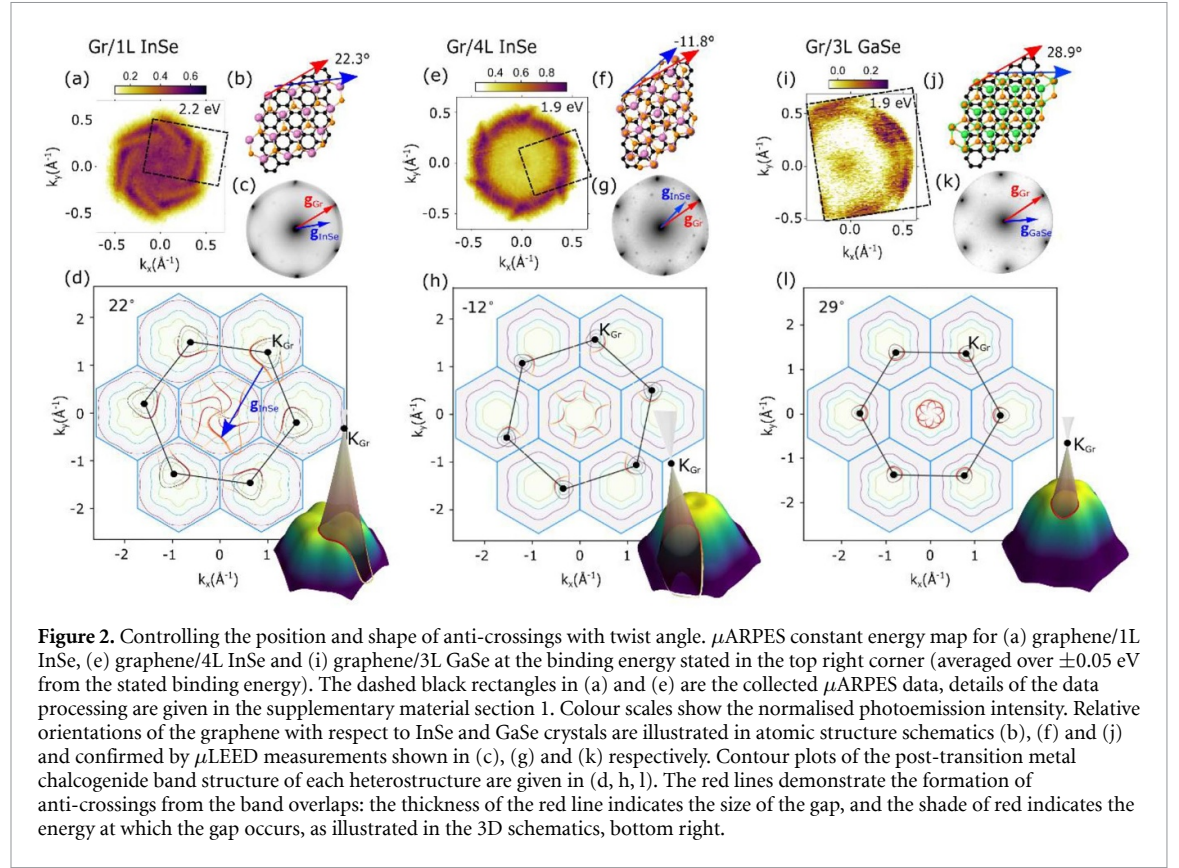


Figure 1. Anti-crossings observed in the valence band structure of graphene/1L InSe heterostructure. (a) Left: μ ARPES energy-momentum slice along the Γ - K_{Gr} direction, passing through the InSe Brillouin zone boundary (blue vertical line) (K_{Gr} denotes the corner of graphene’s Brillouin zone). Overlaid on the left are theoretical predictions for the isolated InSe bands (blue dashed) and graphene π band (red dashed). The black dashed line indicates the position of the graphene π band when folded into the 1st Brillouin zone of InSe (note that the folded graphene π band does not originate near the Dirac point and so is at higher binding energy). Right: mirrored, the double-differential of the same spectra shown on the left. InSe is at a twist angle of $22.3 \pm 0.6^\circ$ with respect to graphene. An anti-crossing is highlighted by the purple box on the right and a ghost anti-crossing by the black box. Scale bar, 0.5 \AA^{-1} . (b) 3D schematic of the uppermost valence band of InSe and graphene π band; red/yellow lines highlight the position of overlap. Blue and black hexagons represent InSe and graphene Brillouin zones respectively. The grey plane marks the slice of energy-momentum space covered by the μ ARPES data in (a). The red arrow indicates folding of an anti-crossing in the second Brillouin zone of InSe to a ghost anti-crossing in the first Brillouin zone. Inset: atomic schematic cross-section of the graphene/1L InSe/graphite 2D heterostructure.

supplementary material, section 1 (available online at <https://stacks.iop.org/2DM/8/015016/mmedia>). Low energy electron diffraction from a submicrometre spot (μ -LEED), taken at the same position on the sample as the μ ARPES measurements (see low energy electron microscopy (LEEM) image in supplementary material, section 2), gives diffraction peaks from both the graphene and InSe layers. In-plane, InSe has a hexagonal lattice with lattice parameter, $a_{InSe} = 4.00 \text{ \AA}$ [20], 60% larger than that of graphene, $a_{gr} = 2.46 \text{ \AA}$. When stacked with a twist angle θ between the layers, they form an incommensurate structure where the Brillouin zone corners in the graphene layer, K_{Gr} , lie in the second Brillouin zone of



the InSe layer. By identifying the LEED peak positions for both materials, we find the twist angle between their crystalline lattices $\theta = 22.3 \pm 0.6^\circ$. In figure 2(d) we plot a contour map of the InSe UVB energy in its first and second Brillouin zone, with the first Brillouin zone of graphene overlaid (black hexagon). As shown in the three-dimensional band schematic, figure 1(b), in monolayers of InSe the UVB dispersion takes the shape of an inverted ‘Mexican hat’ [21] around the zone centre, Γ , with the valence band maximum (VBM) close to but not at Γ , and the band disperses to a minimum at the zone corner K_{InSe} . By contrast, the UVB in graphene forms the characteristic Dirac cones, meeting the conduction band at the six Dirac points at the zone corners, K_{Gr} . Band anti-crossings occur where the graphene and InSe bands would have been coincident. Their position is shown on the contour map by red lines, drawn using an interpolation formula [22], which map out distorted-triangular closed curves around the Dirac cones, in the second Brillouin zone of InSe. Umklapp scattering by an InSe reciprocal lattice vector, G_{InSe} , replicates these anti-crossings in the first Brillouin zone of InSe.

This emphasizes the difference between this interlayer Umklapp process and the Moiré phenomena previously reported in systems such as twisted bilayer graphene where a Moiré superlattice potential creates replica bands shifted by the Moiré wave vector $K_M = G_{\text{InSe}} - G_{\text{graphene}}$ and interaction between the primary and replica bands creates flat bands, as previously

observed by μ ARPES [11, 12]. Here, no replica bands are apparent, suggesting negligible Moiré superlattice potential, and the ghost anti-crossings are found by mapping the band anti-crossings by G_{InSe} not K_M , similar to previous ARPES measurements of incommensurate twisted bilayer graphene [23]. There are also similarities to the back-folding of bands by charge density waves and spin density waves [24–26], where ARPES has revealed clear anti-crossings between the primary and replica bands even when the replica bands themselves are weak. Here, however, rather than stemming from a new ordered phase within the material, the observed ghost anti-crossings can be explained by interlayer Umklapp scattering. However, to reproduce the experimentally measured pattern, the angular dependence of the interlayer hybridization must also be considered.

To do this, we employ a method developed [17, 27] for the description of ARPES intensity maps of graphene [28] and tunnelling between 2D crystals [9, 29]. It uses a plane wave decomposition of Bloch states of electrons in the graphene bands, and in the UVB of InSe, then describes the variation of the interlayer hybridisation parameters across the relevant part of the Brillouin zone by projecting the plane wave components with the coinciding wave vectors. The states involved in the hybridisation are related by the umklapp condition, $\mathbf{q} = \xi K_n - G_{\text{InSe}} + \mathbf{p}$ (where $\xi = +$ or $-$ from the two inequivalent valleys in graphene and $n = 0, 1$ and 2 indexes the three equivalent valleys, $\mathbf{p} = (p_x, p_y)$ is the valley

momentum of graphene, and \mathbf{q} is the momentum of the InSe counted from the Brillouin zone centre with $\mathbf{q} \ll \mathbf{G}_{\text{InSe}}$. Along the six lines that satisfy this condition (figure 2(d)), counted by integer $\mu = 0$ to 5 counter-clockwise, hybridisation between the graphene-InSe bands leads to the anti-crossing of their dispersions, splitting them apart by

$$\delta\epsilon \propto \left| \sin \left(\varphi_{\vec{p}} - \frac{\pi}{3} \mu \right) \right|, \quad (1)$$

where $\varphi_{\vec{p}} = \arctan(p_y/p_x)$ describes the direction of valley momentum. The angular dependence highlighted in equation (1) is the result of sublattice composition-n (AB) of electron states in graphene (for details see Methods), which has been seen in twist-controlled electron tunnelling in graphene/hBN/graphene heterostructures [9]. On the plot in figure 2(d), this variation of the interlayer hybridisation factor, $\delta\epsilon$, is shown by the thickness of the red lines. Taking this variation into account, the resultant momentum-space images of the anti-crossings qualitatively reproduce the experimental behaviour observed in figure 2(a).

The pattern of anti-crossings is dependent on θ (see supplementary material, section 3), and can be observed in other 2D heterostructures. Figure 2(e) shows the mini-gap pattern apparent in a constant energy slice taken on graphene-capped 4L InSe, with $\theta = 11.8 \pm 0.1^\circ$ determined by μ -LEED. Again, a contour plot showing the expected position of the ghost anti-crossings, figure 2(h), calculated by umklapp scattering from the overlap contours in the second Brillouin zone of InSe, qualitatively reproduces the experimental measurement. We observe the same effect in a constant energy slice from a 2D heterostructure of graphene-capped 3L GaSe (figure 2(i)), where μ -LEED was used to determine $\theta = 28.9 \pm 0.7^\circ$. The minigap pattern observed in the experimental measurement again agrees with the expected pattern, figure 2(l). The ‘ghost’ anti-crossing is observed in the energy-momentum spectra shown in supplementary material, section 4.

The interlayer hybridization factor, $\delta\epsilon$, can be determined from fitting the band dispersions where the InSe UVB meets the graphene π band. An ARPES energy-momentum slice of the anti-crossing, from the same sample as figure 2(e), is shown in figure 3. The band mixing and anti-crossing gap are clear in the data twice-differentiated with respect to energy, the right spectra of figure 3. Band positions were found by fitting energy distribution curves around the anti-crossing, and from these band positions the interlayer hybridization factor was found, $\delta\epsilon = 0.45 \pm 0.02$ eV. The dispersion and magnitude of this anti-crossing are consistent with the corresponding ghost anti-crossing, as shown in figure 3(b) from a region of graphene covering 4L InSe. This clear ghost anti-crossing in 4L InSe demonstrates that the effect is not limited to

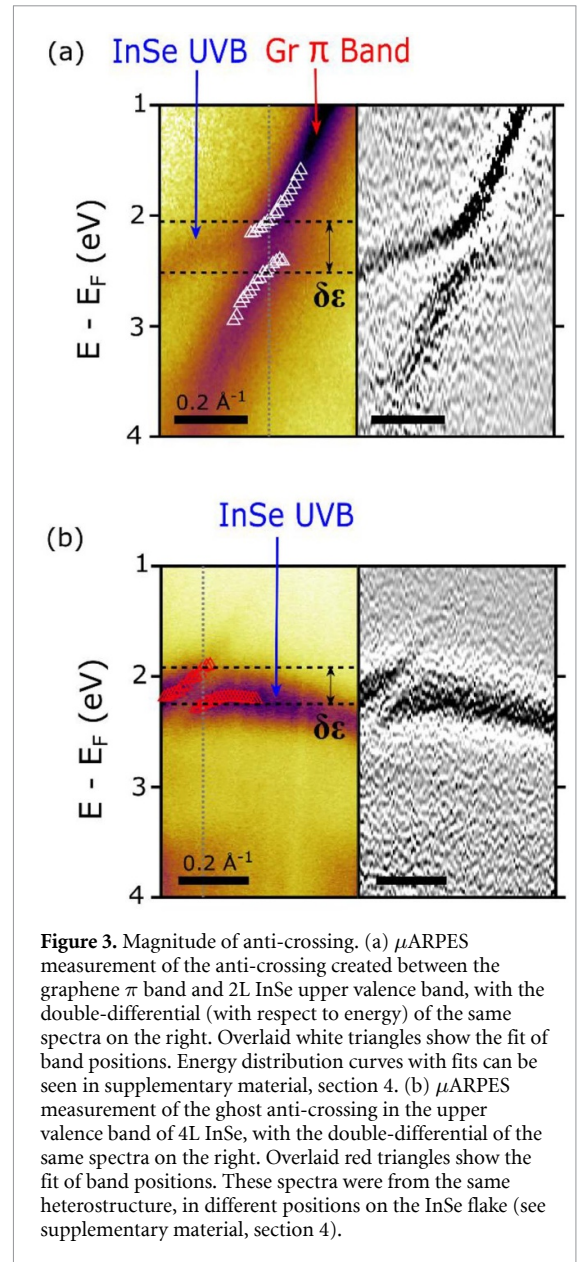
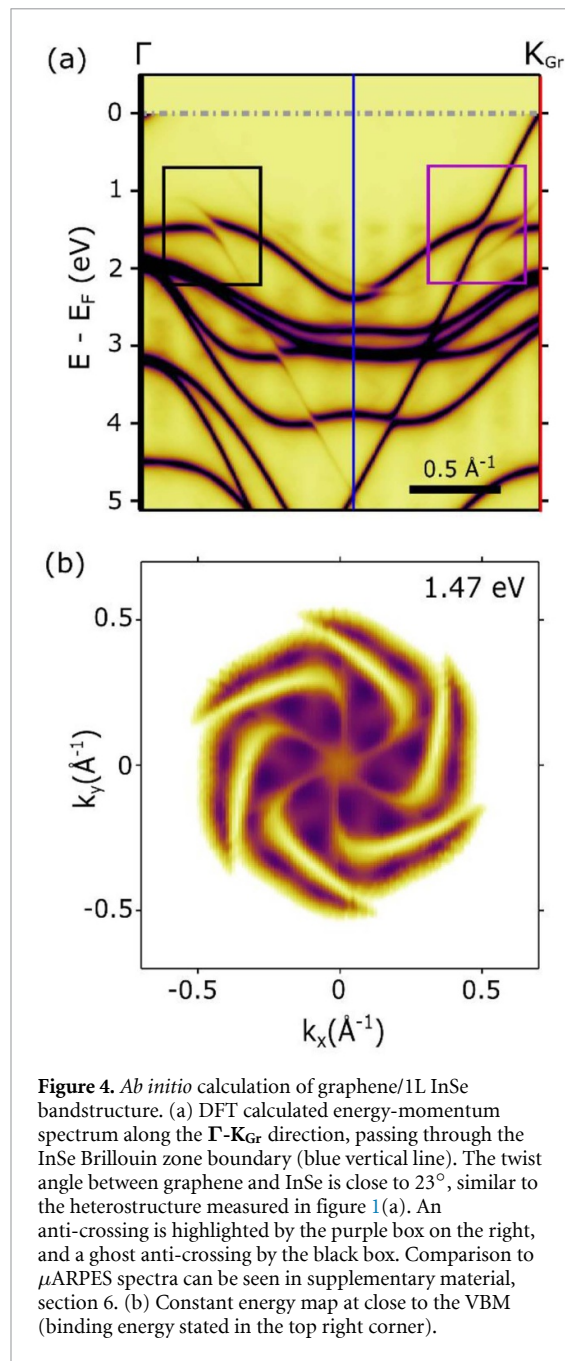


Figure 3. Magnitude of anti-crossing. (a) μ ARPES measurement of the anti-crossing created between the graphene π band and 2L InSe upper valence band, with the double-differential (with respect to energy) of the same spectra on the right. Overlaid white triangles show the fit of band positions. Energy distribution curves with fits can be seen in supplementary material, section 4. (b) μ ARPES measurement of the ghost anti-crossing in the upper valence band of 4L InSe, with the double-differential of the same spectra on the right. Overlaid red triangles show the fit of band positions. These spectra were from the same heterostructure, in different positions on the InSe flake (see supplementary material, section 4).

monolayer materials. Note that figures 3(a) and (b) were acquired from different areas of the same graphene on InSe heterostructure with the same orientations of graphene and InSe flakes but differing InSe thickness (see supplementary material, section 5).

Ghost anti-crossings are also apparent in *ab initio* predictions of the band structure of the composite graphene/InSe stack, further confirming that they are an inherent feature of the electronic structure. Using linear-scaling DFT (LS-DFT) [30, 31], we studied graphene on monolayer InSe at 23° , corresponding to a supercell of 698 atoms (see Methods and supplementary material, section 6). Using previously reported tools to project the electronic structure into the primitive cells of each layer [32], simulated spectra of the valence bands of the composite structure were constructed. A momentum slice plotted along Γ to \mathbf{K}_{Gr} (figure 4(a)) shows mini-gaps at anti-crossings of



InSe valence bands with the graphene π band, as well as anti-crossings with interlayer umklapp scattered π bands. These are not present in the electronic structures of the separated layers. A simulated constant energy slice (figure 4(b)) shows the same characteristic vortex as observed experimentally and as predicted by the analytical model above. Changes in the measured and simulated pattern with binding energy are compared in supplementary material, section 7.

3. Conclusion

In summary, our data present evidence for interlayer umklapp scattering in 2D heterostructures. The ghost anti-crossings created near the VBM of monolayer

InSe demonstrate points of strong coupling with the adjacent graphene layer, with their position controlled by the relative orientation between the layers. Further control could be gained through changing band-alignments, using chemical doping or a perpendicular electric field [33]. By selecting suitable 2DMs pairs, it should thus be possible to engineer strong mixing of their electronic states at or near the band edges of many 2D semiconductors, or near the Fermi-level of metals and semi-metals, giving a new tool for band structure engineering. This interlayer umklapp scattering should not be limited to band hybridisation, and we expect it also to manifest in further novel electron, phonon and photon interactions in 2D heterostructures.

4. Methods

4.1. Sample fabrication

Bulk rhombohedral γ -InSe crystals, purchased from 2D Semiconductors and grown using the vertical Bridgman method, were mechanically exfoliated down to thin (1L–10L) crystals on a silicon oxide substrate. Using the PMMA dry peel transfer technique [34], monolayer graphene was used to pick-up and stamp InSe crystals onto either graphite or hBN, each of which was laterally large ($>50 \mu\text{m}$), thin ($<50 \text{ nm}$) and positioned on a (3 nm) Ti/(20 nm) Pt-coated highly n-doped silicon wafer. Both heterostructure samples were annealed to 150° for 1 h in order to remove impurities via the self-cleaning mechanism [6]. All that is described above took place within an Ar glove box to prevent sample degradation. The same samples were used for both μ ARPES and μ LEED measurements.

4.2. μ ARPES

μ ARPES spectra were acquired from the Spectromicroscopy beamline of the Elettra light source [35]. A low energy (27 eV), linearly polarised photon beam was focused onto the sample surface using Schwarzschild objectives. The beam had a submicrometre spot size ($\sim 600 \text{ nm}$) and was at an incident angle of 45° to the sample surface (linearly polarised at 45° to the sample surface). To perform ARPES, photoemitted electrons were collected by an internal moveable hemispherical electron analyser and 2D detector with an energy and momentum resolution of $\sim 50 \text{ meV}$ and $\sim 0.03 \text{ \AA}^{-1}$. Before analysis, samples were annealed for $>6 \text{ h}$ at up to around 625 K in ultra-high vacuum. The correct position on the sample was found by comparing an optical image of the specimen to scanning photoemission microscopy images acquired on the beamline before ARPES measurements. Energy-momentum slices along the high symmetry directions of the Brillouin zones were acquired by measuring a series of closely spaced

detector slices and interpolating the spectra. The constant energy maps, $I(\mathbf{k}_x, \mathbf{k}_y)$, around Γ were extracted from three-dimensional energy-momentum maps, $I(E, \mathbf{k}_x, \mathbf{k}_y)$ and averaged over an energy range of 0.04 eV. The sample temperature during measurement was ~ 100 K.

4.3. μ LEED

μ LEED patterns were acquired on the LEEM at the Nanospectromicroscopy beamline of the Elettra light source [36]. A well-collimated beam of low energy electrons from a LaB₆ electron-gun was focused on to the sample, the electron energy being set by applying a voltage bias to the sample stage. An e-beam footprint on the sample of only 500 nm was obtained by inserting an illumination limiting aperture in the microscope optical path. Magnified images of the diffraction pattern produced by elastically backscattered electrons were acquired using a 2D detector and CCD. The diffraction pattern shown in figure 2(c) is an average of multiple diffraction patterns collected over an incident electron energy range of 30–60 eV in steps of 2 eV. The diffraction pattern shown in figure 2(g) is an average of multiple diffraction patterns collected over an incident electron energy range of 27–60 eV in steps of 1 eV. The diffraction pattern shown in figure 2(k) was collected with an incident electron energy of 55 eV.

4.4. Modelling of sublattice effects on resonant hybridization between graphene and InSe

We used a plane wave decomposition of Bloch states of electrons in the graphene bands, and in the UVB of InSe, then projected the plane wave components with the coinciding wave vectors. For graphene, the relevant parts of the spectrum appear in the vicinity of Dirac points near K ($\xi = +$) and K' ($\xi = -$) valleys, where the plane wave decomposition, that involves the set of smallest wave vectors $\xi \vec{K}_n + \vec{p}$, related by the reciprocal lattice vectors for graphene, reads

$$\psi_\xi \approx N(|z|) \sum_{\mathbf{K}_{Gr}} \left[1 + s\xi e^{i\xi(\varphi_{\vec{p}} - \frac{2\pi}{3}n)} \right] e^{i(\xi \vec{K}_{Gr} + \vec{p}) \cdot \vec{r}}.$$

Here, $\varphi_{\vec{p}} = \arctan(p_y/p_x)$ describes the direction of valley momentum $\vec{p} = (p_x, p_y)$ of electrons in graphene, $s = +1$ for conduction band and $s = -1$ for valence band branch of dispersion ($s = -1$ is the one relevant for resonant mixing with InSe valence band states), $\vec{r} = (x, y)$, and $N(|z|)$ takes into account the decay of the 2D plane wave amplitude away from the crystal. The factor $\left[1 + s\xi e^{i\xi(\varphi_{\vec{p}} - \frac{2\pi}{3}n)} \right]$ accounts for the interference of the contributions to the ‘vacuum’ planes coming from P_z orbitals of carbons on two (A&B) sublattices of honeycomb graphene [17]. For InSe, we concentrate on the UVB dispersion in the vicinity of its top near the BZ centre, where the electron states come mostly from S and P_z orbitals of chalcogen atoms [37]. This prescribes the

plane wave decomposition for the top valence band state in monolayer InSe,

$$\Psi \approx f(|z|) e^{i\vec{q} \cdot \vec{r}} + g(|z|) \sum_{\mu} e^{i(\vec{G}_{InSe} + \vec{q}) \cdot \vec{r}},$$

where \vec{G}_{InSe} is the first star of InSe reciprocal lattice vectors and \vec{q} is counted from the BZ centre ($q \ll G_{InSe}$). After projecting the plane waves in the two crystals, we find that the states involved in the hybridisation are related by the Umklapp condition, $\vec{q} = \xi \vec{K}_n - \vec{G}_{InSe} + \vec{p}$, and the variation of their interlayer coupling across the BZ is described by $h(\vec{q}) \propto \left[1 + s\xi e^{i\xi(\varphi_{\vec{p}} - \frac{2\pi}{3}n)} \right]$. Due to the decay of the electronic wave functions away from each crystal, which is even faster for the $\vec{G}_{InSe} + \vec{q}$ plane wave components ($g(|z|)$) than for the \vec{q} component ($f(|z|)$), *i.e.* $g(|z|) \ll f(|z|)$ at distances $|z|$ longer than the Bohr radius), the hybridisation of graphene and InSe bands would be negligibly weak, unless it satisfies the resonant condition, $\varepsilon_{InSe}(\vec{q}) = \varepsilon_{gr}(\vec{p})$. Along the six lines identified by such crossings, counted by integer $\mu = 0$ to 5 counter-clockwise, graphene-InSe bands hybridisation leads to the anti-crossing of their dispersions, splitting them apart by $\delta\varepsilon = 2|h| \propto |\sin(\varphi_{\vec{p}} - \frac{\pi}{3}\mu)|$, leading to equation (1) in the main text. Values of $\vec{G}_{InSe} = 1.73 \text{ \AA}^{-1}$ and $\vec{G}_{GaSe} = 1.85 \text{ \AA}^{-1}$ were used, consistent with literature values for these materials [38].

4.5. Ab initio calculations

LS-DFT calculations in the Projector Augmented Wave formalism [30, 39] were used to model the InSe/Gr heterostructure, using the ONETEP code [31]. Further details are given in supplementary material, section 3.

Acknowledgments

This work was supported by EPSRC (grants EP/N509565/1, EP/P01139X/1, EP/N010345/1, and EP/L01548X/1 along with the CDT Graphene-NOWNANO and the EPSRC Doctoral Prize Fellowship), the European Graphene Flagship Project, ERC Synergy Grant Hetero2D, the ARCHER National UK Supercomputer RAP Project e547, Royal Society URF, and Lloyd Register Foundation Nanotechnology grant. We acknowledge the use of Athena at HPC Midlands+, which was funded by the EPSRC through Grant No. EP/P020232/1, as part of the HPC Midlands+ consortium, and computing resources provided by the Scientific Computing Research Technology Platform of the University of Warwick. The research leading to this result has been supported by the project CALIPSOplus under Grant Agreement 730872 from the EU Framework Programme for Research and Innovation HORIZON 2020. The authors declare no competing interests. The research data supporting this publication can be accessed via

the University of Warwick's Research Archive Portal,
<https://wrap.warwick.ac.uk/143302>.

ORCID iDs

Johanna Zultak  <https://orcid.org/0000-0003-0901-038X>

Neil R Wilson  <https://orcid.org/0000-0002-2592-3077>

References

- [1] Bloch F 1928 Über die quantenmechanik der elektronen in kristallgittern *Z. Phys.* **52** 555–600
- [2] Peierls R 1935 Quelques propriétés typiques des corps solides *Ann. l'I. H. P.* **5** 177–222 (http://www.numdam.org/item/AIHP_1935__5_3_177_0/)
- [3] Wallbank J R *et al* 2019 Excess resistivity in graphene superlattices caused by umklapp electron–electron scattering *Nat. Phys.* **15** 32–36
- [4] Alexeev E M *et al* 2019 Resonantly hybridized excitons in moiré superlattices in van der Waals heterostructures *Nature* **567** 81–86
- [5] Rooney A P, Kozikov A, Rudenko A N, Prestat E, Hamer M J, Withers F, Cao Y, Novoselov K S and Katsnelson M I 2017 Observing Imperfection in atomic interfaces for van der Waals heterostructures *Nano Lett.* **17** 5222–8
- [6] Haigh S J, Gholinia A, Jalil R, Romani S, Britnell L, Elias D C, Novoselov K S, Ponomarenko L A, Geim A K and Gorbachev R 2012 Cross-sectional imaging of individual layers and buried interfaces of graphene-based heterostructures and superlattices *Nat. Mater.* **11** 764–7
- [7] Dean C R *et al* 2010 Boron nitride substrates for high-quality graphene electronics *Nat. Nanotechnol.* **5** 722–6
- [8] Fallahazad B *et al* 2015 Gate-tunable resonant tunneling in double bilayer graphene heterostructures *Nano Lett.* **15** 428–33
- [9] Woods C R *et al* 2014 Twist-controlled resonant tunnelling in graphene/boron nitride/graphene heterostructures *Nat. Nanotechnol.* **9** 808–13
- [10] Bistritzer R and MacDonald A H 2011 Moiré bands in twisted double-layer graphene *Proc. Natl Acad. Sci. USA* **108** 12233–7
- [11] Lisi S *et al* 2020 Direct evidence for flat bands in twisted bilayer graphene from nano-ARPES *arXiv:2002.02289*
- [12] Utama M I B *et al* 2019 Visualization of the flat electronic band in twisted bilayer graphene near the magic angle twist *arXiv:1912.00587* 2–8
- [13] Pletikosić I, Kralj M, Pervan P, Brako R, Coraux J, N'Diaye A T, Busse C and Michely T 2009 Dirac cones and minigaps for graphene on Ir(111) *Phys. Rev. Lett.* **102** 056808
- [14] Varykhalov A, Sánchez-Barriga J, Shikin A M, Biswas C, Vescovo E, Rybkin A, Marchenko D and Rader O 2008 Electronic and magnetic properties of quasifreestanding graphene on Ni *Phys. Rev. Lett.* **101** 157601
- [15] Coy Diaz H, Avila J, Chen C, Addou R, Asensio M C and Batzill M 2015 Direct observation of interlayer hybridization and Dirac relativistic carriers in graphene/MoS₂ van der Waals heterostructures *Nano Lett.* **15** 1135–40
- [16] Pierucci D *et al* 2016 Band alignment and minigaps in monolayer MoS₂-graphene van der Waals heterostructures *Nano Lett.* **16** 4054–61
- [17] Mucha-Kruczyński M, Tsyplatyev O, Grishin A, McCann E, Fal'ko V I, Bostwick A and Rotenberg E 2008 Characterization of graphene through anisotropy of constant-energy maps in angle-resolved photoemission *Phys. Rev. B* **77** 195403
- [18] Bostwick A, Ohta T, Seyller T, Horn K and Rotenberg E 2007 Quasiparticle dynamics in graphene *Nat. Phys.* **3** 36–40
- [19] Wilson N R *et al* 2017 Determination of band offsets, hybridization, and exciton binding in 2D semiconductor heterostructures *Sci. Adv.* **3** e1601832
- [20] Rigoult J, Rimsky A and Kuhn A 1980 Refinement of the 3R γ -indium monoselenide structure type *Acta Crystallogr. B* **36** 916–8
- [21] Hamer M J *et al* 2019 Indirect to direct gap crossover in two-dimensional InSe revealed by angle-resolved photoemission spectroscopy *ACS Nano* **13** 2136–42
- [22] Zólyomi V, Drummond N D and Fal'ko V I 2014 Electrons and phonons in single layers of hexagonal indium chalcogenides from ab initio calculations *Phys. Rev. B* **89** 205416
- [23] Yao W *et al* 2018 Quasicrystalline 30° twisted bilayer graphene as an incommensurate superlattice with strong interlayer coupling *Proc. Natl Acad. Sci.* **115** 6928–33
- [24] Perfetti L, Gloor T A, Mila F, Berger H and Grioni M 2005 Unexpected periodicity in the quasi-two-dimensional Mott insulator 1T-TaS₂ revealed by angle-resolved photoemission *Phys. Rev. B* **71** 153101
- [25] Rotenberg E, Freelon B K, Koh H, Bostwick A, Rossnagel K, Schmid A and Kevan S D 2005 Electron states and the spin density wave phase diagram in Cr(1: 1 0) films *New J. Phys.* **7** 114–114
- [26] Nicholson C W, Schwier E F, Shimada K, Berger H, Hoesch M, Berthod C and Monney C 2020 Role of a higher-dimensional interaction in stabilizing charge density waves in quasi-one-dimensional NbSe₃ revealed by angle-resolved photoemission spectroscopy *Phys. Rev. B* **101** 045412
- [27] Lane T L M, Wallbank J R and Fal'ko V I 2015 Twist-controlled resonant tunnelling between monolayer and bilayer graphene *Appl. Phys. Lett.* **107** 203506
- [28] Ohta T, Bostwick A, Seyller T, Horn K and Rotenberg E 2006 Controlling the electronic structure of bilayer graphene *Science* **313** 951–4
- [29] Novoselov K S, Mishchenko A, Carvalho A and Castro Neto A H 2016 2D materials and van der Waals heterostructures *Science* **353** aac9439
- [30] Hine N D M 2017 Linear-scaling density functional theory using the projector augmented wave method *J. Phys.: Condens. Matter.* **29** 024001
- [31] Prentice J C A *et al* 2020 The ONETEP linear-scaling density functional theory program *J. Chem. Phys.* **152** 174111
- [32] Constantinescu G C and Hine N D M 2015 Energy landscape and band-structure tuning in realistic MoS₂/MoSe₂ heterostructures *Phys. Rev. B* **91** 195416
- [33] Bao X, Ou Q, Xu Z-Q, Zhang Y, Bao Q and Zhang H 2018 Band structure engineering in 2D materials for optoelectronic applications *Adv. Mater. Technol.* **3** 1800072
- [34] Ponomarenko L A *et al* 2011 Tunable metal-insulator transition in double-layer graphene heterostructures *Nat. Phys.* **7** 958–61
- [35] Dudin P, Lacovig P, Fava C, Nicolini E, Bianco A, Cautero G and Barinov A 2010 Angle-resolved photoemission spectroscopy and imaging with a submicrometre probe at the SPECTROMICROSCOPY-3.2L beamline of Elettra *J. Synchrotron Radiat.* **17** 445–50
- [36] Menteş T O, Zamborlini G, Sala A and Locatelli A 2014 Cathode lens spectromicroscopy: methodology and applications *Beilstein J. Nanotechnol.* **5** 1873–86
- [37] Magorrian S J, Zólyomi V and Fal'ko V I 2016 Electronic and optical properties of two-dimensional InSe from a DFT-parametrized tight-binding model *Phys. Rev. B* **94** 245431
- [38] Demirci S, Avazlı N, Durgun E and Cahangirov S 2017 Structural and electronic properties of monolayer group III monochalcogenides *Phys. Rev. B* **95** 115409
- [39] Bloch P E 1994 Projector-augmented plane-wave method *Phys. Rev. B* **50** 17953–79